metals

MDPI

Article

Revealing the Surface and In-Depth Operational Performances of Oxygen-Evolving Anode Coatings: A Guideline for the Synthesis of Inert Durable Anodes in Metal Electrowinning from Acid Solutions

Jovana Bošnjaković [1], Vladimir Panić [1], Maja Stevanović [2], Srecko Stopic [3], Jasmina Stevanović [1], Branimir Grgur [4] and Gavrilo Šekularac [1,*]

[1] Department of Electrochemistry, Institute of Chemistry, Technology and Metallurgy, National Institute of the Republic of Serbia, University of Belgrade, Njegoševa 12, 11000 Belgrade, Serbia; jovana.bosnjakovic@ihtm.bg.ac.rs (J.B.); panic@ihtm.bg.ac.rs (V.P.); jaca@tmf.bg.ac.rs (J.S.)
[2] Innovation Center of Faculty of Technology and Metallurgy, Karnegijeva 4, 11000 Belgrade, Serbia; majas@tmf.bg.ac.rs
[3] IME Process Metallurgy and Metal Recycling, RWTH Aachen University, Intzestraβe 3, D-52072 Aachen, Germany; sstopic@ime-aachen.de
[4] Faculty of Technology and Metallurgy, University of Belgrade, Karnegijeva 4, 11000 Belgrade, Serbia; bngrgur@tmf.bg.ac.rs
* Correspondence: gavrilo@ihtm.bg.ac.rs

Abstract: The electrochemical performances of an oxygen-evolving anode produced by the reactivation of waste Ti substrate by a typical IrO_2-Ta_2O_5 coating are correlated to the textural (non)uniformities of the coating and its exhaustion state. Coating degradation is considered operational loss of the activity in a metal electrowinning process. It was found that (pseudo)capacitive performances can vary over the coating surface by 20–30% and depend on the type of dynamics of the input perturbation: constant through cyclic voltammetry (CV) or discontinuous time-dependent through electrochemical impedance spectroscopy (EIS). CV-EIS data correlation enabled profiling of the capacitive properties through the depth of a coating and over its surface. The correlation was confirmed by the findings for the analysis of coating activity for an oxygen evolution reaction, finally resulting in the reliable proposition of a mechanism for the operational loss of the anode. It was found that the less compact and thicker coating parts performed better and operated more efficiently, especially at lower operational current densities.

Keywords: IrO_2-based anodes; operational efficiency in metal electrowinning; electrochemistry of porous electrodes; distributed electrochemical capacitance; anode disfunction

Citation: Bošnjaković, J.; Panić, V.; Stevanović, M.; Stopic, S.; Stevanović, J.; Grgur, B.; Šekularac, G. Revealing the Surface and In-Depth Operational Performances of Oxygen-Evolving Anode Coatings: A Guideline for the Synthesis of Inert Durable Anodes in Metal Electrowinning from Acid Solutions. *Metals* **2024**, *14*, 1339. https://doi.org/10.3390/met14121339

Academic Editor: Chang Woo Lee

Received: 30 September 2024
Revised: 14 November 2024
Accepted: 22 November 2024
Published: 26 November 2024

1. Introduction

Titanium electrodes with a catalytic coating based on iridium oxide are known to have the best performance for oxygen evolution in industrial electrolysis. These oxygen-evolving anodes (OEAs) are unavoidable in the field of electrogalvanization, water electrolysis, the mining industry, wastewater remediation, impressed current cathodic protection and wastewater electropurification [1–6].

OEAs based on noble metal oxides led to a revolution in electrochemical technologies, owing to their good process stability and excellent catalytic activity [7–9]. However, during the oxygen evolution reaction, simultaneous anodic dissolution of electrochemically active oxide occurs. For example, the much shorter service life of RuO_2-based anodes in comparison with IrO_2-based anode coatings is due to the much lower anodic stability of RuO_2 [10–12]. RuO_2 or IrO_2 in gas-evolving anodes act as electronic catalysts, while TiO_2 and Ta_2O_5 preserve the chemical and mechanical stability of the anode oxide coatings [13–15].

Owing to their stabilizing role, valve metal oxides such as Ta_2O_5 and TiO_2 as well as, for example, SnO_2, which can partially operate as a catalyst, reduce the required catalytic powder production costs of the anodes [16–18]. Comninellis and Vercesi [19] showed that a coating with 70 mol% Ir and 30 mol% Ta on Ti has the best activity for oxygen evolution reactions (OERs) and consequently the longest service life in sulfate solutions [20–22].

Coatings for OEAs can be prepared by different methods, such as thermal decomposition of metallic salts, electrodeposition, sol-gel and the Pechini method [23,24]. The anodes used in industries are usually produced with the thermal decomposition method, due to the low cost and simplicity of the process itself. In thermal decomposition, the corresponding precursor salts dissolved in organic or aqueous solutions are applied onto Ti substrate. The coatings obtained under these conditions suffer from inhomogeneous distribution of their properties, with a large number of cracks and the presence of crystalline IrO_2 aggregates among the cracks and amorphous Ta_2O_5 [25]. The electrocatalytic properties, stability and operational efficiency of the coating are strongly influenced by its surface and microstructural homogeneity degree [26,27]. Consequently, the main challenge is to improve the service life of OEAs in expanding industrial areas, especially at low pH values, moderate electrolyte temperatures and at extremely high current densities [28].

It has been claimed [29] that layered Ir-based coatings of different layer compositions considerably influence the service life of oxygen-evolving electrodes. It follows that the IrO_2 in the surface layer (e.g., IrO_2-Ta_2O_5, 85/15 metal mole ratio) rules the anode service life, which can be considerably improved by 2–2.5 times if coating and support intermediate layers of low IrO_2 contents or even without IrO_2 are introduced. The compositions of the intermediate layers are based on different transition metal oxides. This stabilizing effect of the Ti support and coating intermediate layers was minimally reported for different testing current densities, and it is by far being considerably more pronounced with respect to other increased service life effects by different coating compositions [30,31].

For this certain benefit of the layered coating, it is required to know how the composition and in-depth distribution of the coating's bulk and surface electrochemical uniformity are correlated for a given application of OEAs. In addition, it is fairly unknown what in-depth changes in activity are taking place in the coating upon anode operation and degradation and how these changes affect the OEA's service life. We present an approach which reveals the changes in activity throughout the IrO_2-Ta_2O_5 coating upon its destabilization at different current densities of oxygen evolution at low pH levels. The approach is based on analysis of the dynamic electrochemical responses of a coating of an apparent uniform composition to reveal its in-depth operational changes for future modeling of layered structures. Additionally, surface coating uniformity differences are correlated to an in-depth operational coating profile.

2. Materials and Methods

2.1. Electrode Preparation

An IrO_2-Ta_2O_5 porous coating was prepared with the conventional thermal decomposition method [32]. Before applying the coating, the Ti substrate (industrial waste of commercial OEA, 3 cm × 15 cm × 3 mm) was sandblasted, degreased in acetone (for analysis EMSURE® ACS, ISO, Reag. Ph Eur, Supelco, Merck, Kenilworth, NJ, USA) and washed with deionized water (18MΩ, Merck Millipore, Burlington, MA, USA). The subsequent etching was performed in boiling 10% oxalic acid (ACS reagent grade 99%, Sigma Aldrich, St. Louis, MO, USA) for 2 h in order to remove TiO_2 and generate a surface with a uniform roughness. The precursors, $H_2IrCl_6xH_2O$ (36.0–44.0% Ir, Sigma Aldrich, USA) and $TaCl_5$ (reagent grade 99%, Sigma Aldrich, USA) at an Ir:Ta mole ratio of 70:30 were dissolved in n-butanol (0.2 M), (ACS reagent 99.4%, Sigma Aldrich, USA) and applied in layers to the Ti substrate with the drop casting method. After application, each layer was dried at a temperature of about 50 °C for 5 min, placed in a drying oven at 100 °C for another 5 min and finally annealed in a high-temperature furnace at 500 °C for 15 min. The procedure was repeated four times, with the final annealing lasting for 2 h. The total amount of oxides

applied on the substrate was projected to be 1 mg/cm^2. A digital image of the coated electrode is given in Figure 1.

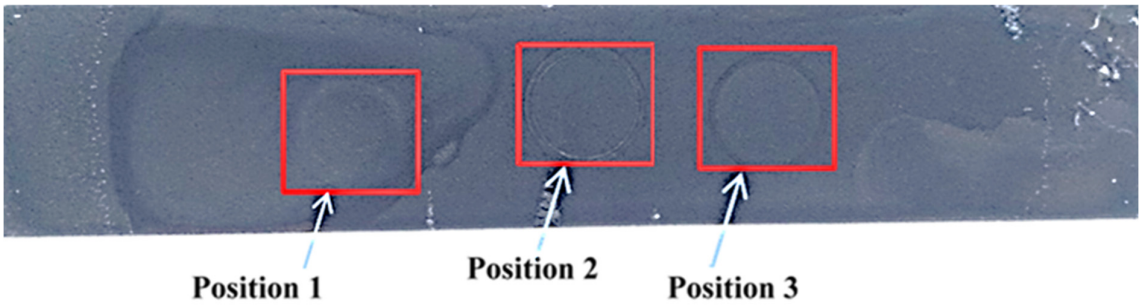

Figure 1. Digital image of coated electrode.

2.2. Electrochemical Measurement

Electrochemical characterization of the as-prepared and exhausted electrode was performed at three randomly selected positions on the electrode's surface using potentiodynamic polarization, cyclic voltammetry (CV), electrochemical impedance spectroscopy (EIS) and an accelerated stability test (AST). All measurements were performed in a 10% H_2SO_4 solution in a high-density polyethylene cell, where a platinum electrode was used as a counter electrode and a saturated calomel electrode (SCE) was the reference. All potentials mentioned are in reference to the SCE scale. The working area of the electrode was 1.33 cm^2, whereas the working area of the counter electrode was 20 cm^2. All measurements were performed using a Biologic—SP 240 potentiostat (BioLogic, Seyssinet-Pariset, France). For anodic potentiodynamic polarization, the scan rate was 2 mV/s. The cyclic voltammetry curves were recorded within a potential window of water stability at a scan rate of 50 mV/s for the 11th steady state cycle. For the EIS measurements, an AC sine signal amplitude of the root mean square of 10 mV was applied around the open circuit potential in a frequency range of 10 mHz–1 MHz. The impedance spectroscopy data obtained were fitted to an appropriate equivalent electrical circuit using ZView® software (version 3.2b).

The AST was conducted under galvanostatic electrolysis conditions, with a current density of 2.0 or 3.0 A/cm^2 at a controlled temperature of 48 °C. The tested electrode was used as the anode, and a platinum wire was used as the cathode. The voltage between the anode and cathode was monitored and recorded. When the voltage reached approximately a 50% increase with respect to the initial voltage of about 6.5 V (set below the potential of the Ti substrate's oxidative breakthrough), the tested electrode was considered to have reached the end of its service life (exhausted electrode). Under the applied conditions, the service life of the prepared electrode was found to be roughly 100 h.

Three randomly selected positions on the electrode's surface were studied to determine the performance uniformity of the coating.

3. Results

Figure 2 shows the cyclic voltammograms (CVs) of the prepared IrO_2-Ta_2O_5 coating at three surface positions on the coating surface before and after the accelerated stability test (AST). The CV responses before and after the AST, as well as all others, were collected from the same positions to check the surface uniformity of the coating's properties. The CVs were of typical shapes and features for noble or transition metal oxide coatings on Ti, with redox peaks in the range from 0.6 to 0.8 V, which is assignable to Ir(III)/Ir(IV) pseudocapacitive redox transitions [32,33]. Figure 2d shows the corresponding voltammetric capacitances, which were assumed to be proportional to the number of active sites in the porous coating accessible via the applied CV dynamic conditions. The pseudocapacitive characteristics were of a moderately homogeneous distribution over the coating's surface; the difference among the three different positions was below 20%. The values at different positions, although randomly chosen, show that positions 1 and 3 reflected the far ends of the characteristics, with position 2 fairly reflecting average characteristics.

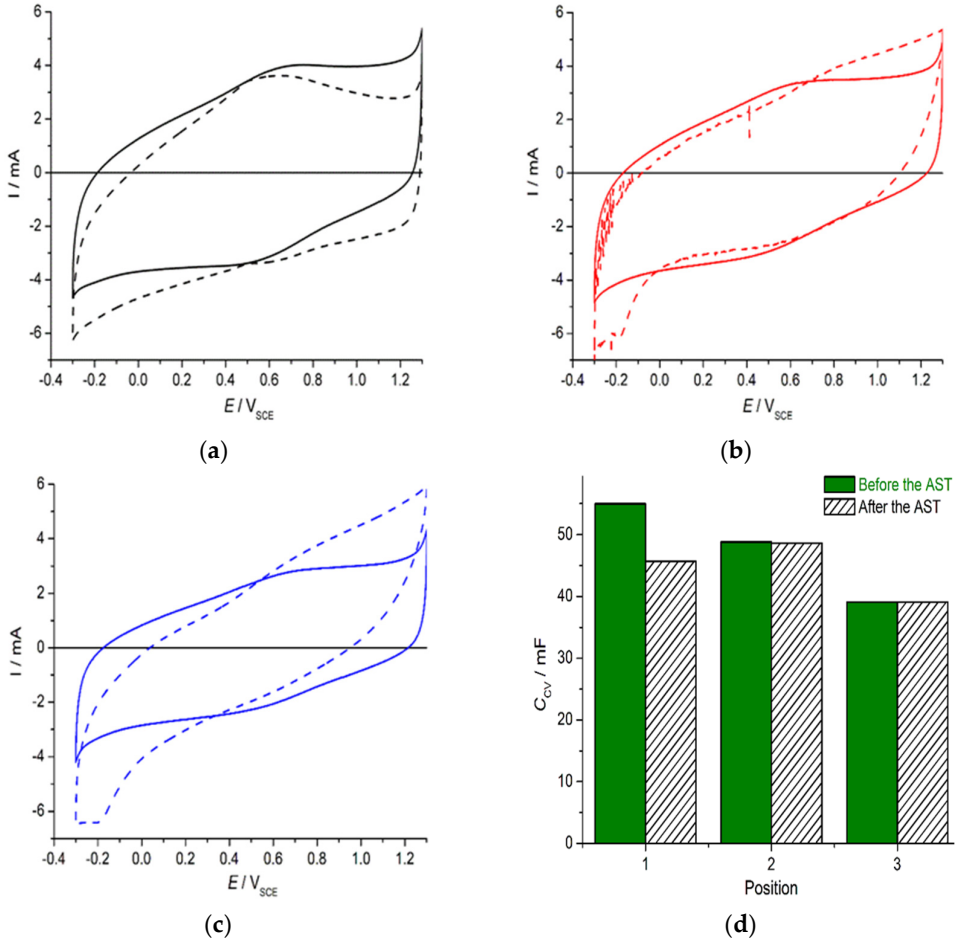

Figure 2. Cyclic voltammograms of IrO_2-Ta_2O_5 coatings on Ti substrate recorded before (full line) and after (dashed line) the accelerated stability test (AST) at positions 1–3 ((**a**–**c**), respectively). (**d**) Voltammetric capacitances calculated from the curves in (**a**–**c**).

The number of active sites (coating composition) as well as their distribution and accessibility throughout the porous layer (coating porosity) affect the pseudocapacitive characteristics [34,35]. The former causes the maximal coating performances at the applied composition, while the compact coating surface layer with a small real surface area can be of a lower coating capacitance. Hence, local deviations in the surface coating composition from the nominal composition can produce lower capacitances at the more compact positions (positions 2 and 3), whereas a less compact coating morphology at position 1 can cause a higher capacitance due to the higher number of accessible active sites from the coating's interior.

Another insight into the differences between the surface positions comes from the comparison of the voltammetric capacitances registered after the AST (Figure 2d). The shapes of the CVs with their main features appeared to be unaffected but were clearly tilted with respect to the CVs of the as-prepared coating. This indicates that the coating resistance increased upon application of the AST, being most pronounced for the lowest initial capacitance at position 3. The tilt was not followed by a decrease in voltammetric capacitance, except to some degree for position 1. It can be mentioned that less pronounced surface coating exhaustion during the AST at the initially less compact position 1 did not uncover much of the internal active sites, as was the case for positions 2 and 3. The more compact surface was relatively more exhausted, which allowed the unhindered access to initially loose internal active sites at positions 2 and 3 upon the AST being carried out. The unaffected capacitance values during the AST indicate that active sites, possibly not being distributed along the surface evenly, might have been evenly distributed through

the coating's bulk. Consequently, the relative difference between the capacitance values at the three positions after the AST decreased to 12% at most, with respect to 20% for the as-prepared coating state.

To prove and analyze further the proposed operational changes in the coating's structure/performance relationship, the impedance response of the coating was registered to discretize its electrochemical parameters through the coating. Figure 3 shows the Bode plots of the EIS data, with the corresponding impedance and capacitance complex plane plots as insets. EIS data from the high-frequency domain of the as-prepared coating obeyed the capacitive-like response down to several hundreds of mHz in the form of well-resolved capacitive loops, with the sizes following the order indicated by the CV response. At the lowest frequencies, the capacitive response resembled the distributed resistor–capacitor in series, thus indicating the discretized time constants of the layers in the coating interior. This manifested as a tail in the capacitance complex plane plots and a phase angle peak of about 0.1 Hz in the Bode plots, which appeared at somewhat higher frequencies for positions 2 and 3 (noted in the CV analysis as being more compact). This agrees with the CV finding that position 1 had a less compact structure (with wider cracks and pores) with a thin surface layer, whereas the coating interior was of a similar structure to that of positions 2 and 3. This could also explain the registered decrease in CV capacitance upon administering the AST exclusively for position 1. The less compact thin layer was exhausted more and consequently uncovered more of the coating interior for the AST. It follows that, aside from fluctuations in the surface coating compositions among different surface positions, the coating could also be of a distributed thickness. Considering that thermal stress during the coating formation on Ti should increase with the coating thickness, more cracked surface layers could be formed for a thicker coating. The stress should be even more pronounced if the coating is deposited with a layered thermal treatment. The thicker, more cracked coating could produce different performance levels at position 1 through CV and be recognized in the capacitive and distributed elements transition issue for the EIS data.

The coating degradation under the AST almost completely disturbed the clear capacitive response of the as-prepared electrode, with no signs of a high-frequency capacitive loop. The EIS data seemed to obey the distributed elements' behavior in a much wider frequency range, with the appearance of a high-frequency semicircle in the complex plane plot, as is typical for coating failures in the AST [36]. The semicircle features differed for different surface positions, being well resolved at position 1 with a clear phase angle peak at approximately 4 kHz and much like the shoulder extending from position 2 to position 3. The corresponding phase angle feature was moved to lower frequencies. If it is assumed that the semicircle is related to an IrO_2-deficient surface coating layer [37], then it can be noted that the layer was best defined and the least compact (appearing at the highest frequency) at what was the least compact surface initially (position 1). The discrete EIS feature caused by coating degradation is seen as resolution of the mid-frequency phase angle region, in addition to the mentioned high- and low-frequency ones. Additional peaks or shoulders, depending on the surface position, appeared. This indicates that the time constants became resolved better upon coating degradation via the AST, since more porous and less compact layers remained.

Bearing in mind the characteristic physicochemical features recognized in the EIS spectra, the equivalent electrical circuit (EEC) which fit the EIS data best was found to be a transmission line of the form $Rs(C_1(R_1(C_2(R_3 \ldots C_{n-1}(R_nC_n)))))$. The resistor R_s bears the parameter of solution resistance, whereas resistor R_i and capacitor C_i represent the coating pore resistance and capacitance of less and less accessible parts of the coating, respectively, from its surface at i = 1 toward the least accessible interiors for i = n. The increasing n can thus be anticipated to be the coating "penetration depth" of the EIS input signal. EIS data for the EEC are given as lines in Figure 3, for which the relative error of the circuit parameters did not exceed 20%, with chi-squared and sum of squares values below 5% and 10^{-4}, respectively. For all coating positions before the AST (as-prepared state), the

EEC of n = 5 returned reliable fitting results, while EECs of n = 6 or 7 (only for the EIS data at position 3) were required to quantify the EIS data after the AST, due to the more pronounced distribution of the time constants.

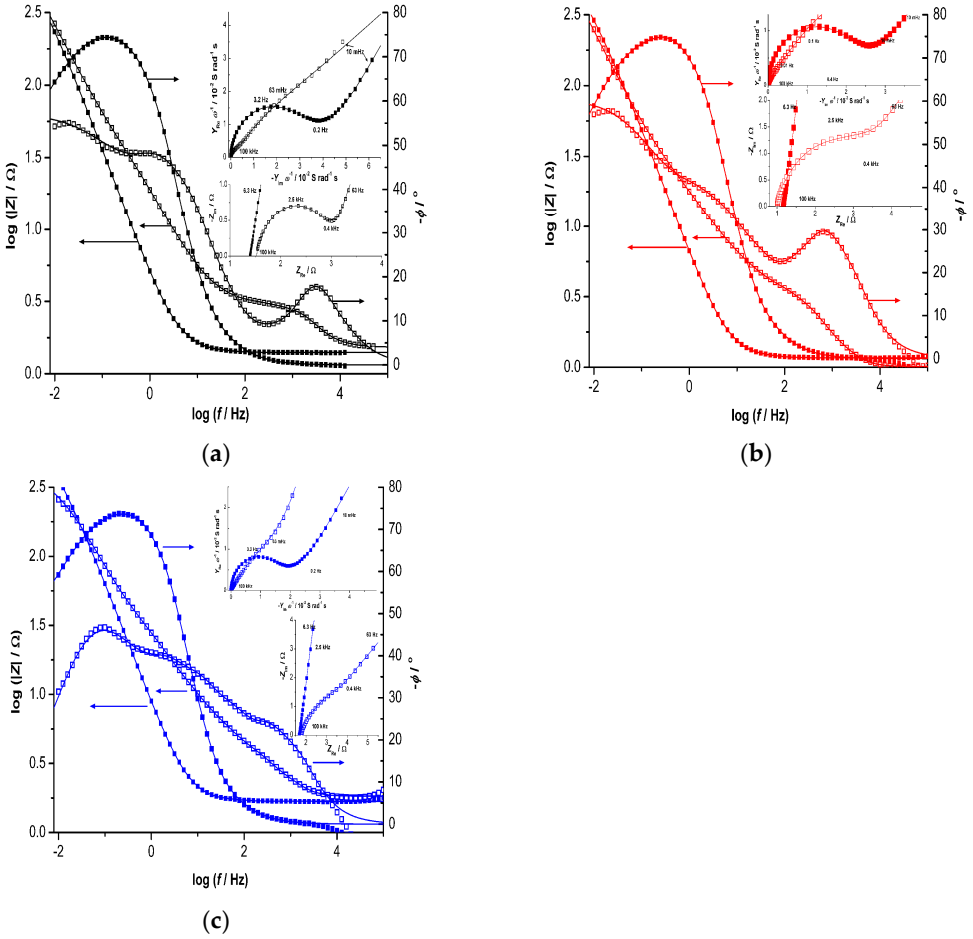

Figure 3. Plots of the EIS data (symbols) of the IrO_2-Ta_2O_5 coating on Ti obtained at the open circuit potential before (full symbols) and after (empty symbols) an accelerated stability test (AST) in 10% H_2SO_4 for coating surface positions 1 (**a**), 2 (**b**) and 3 (**c**). The responses of the transmission line's equivalent electrical circuits are shown as lines.

A 3D distribution of the circuit parameter values as a function of the "effective coating depth" (n value) and surface position is presented in Figure 4 for the as-prepared and exhausted coating.

Both the capacitance and pore resistance of the coating changed within two orders of magnitude through its depth, with opposite trends for the as-prepared and exhausted states. The capacitance was the highest and the resistance the lowest for the coating surface layer with respect to the interior layers. Upon degradation under the AST, the capacitance of the surface layer collapsed by three orders of magnitude, while that of the interior layers seemed to be unaffected. Owing to pore widening during the AST, the pore resistance gradually decreased for all layers except on the surface (n = 2), for which the resistance was doubled in comparison with the as-prepared state. Since the coating surface was exhausted the most, access to the active sites beneath was harder to reach for the capacitive response. These findings clearly indicate that the coating's misfunction was caused exclusively by exhaustion of the active sites from the coating surface, while those in the interior stayed intact. This degradation mechanism would cause poor active material efficiency and indicate the requirement for its in-depth distribution to form its surface allocation under adequate coating preparation conditions.

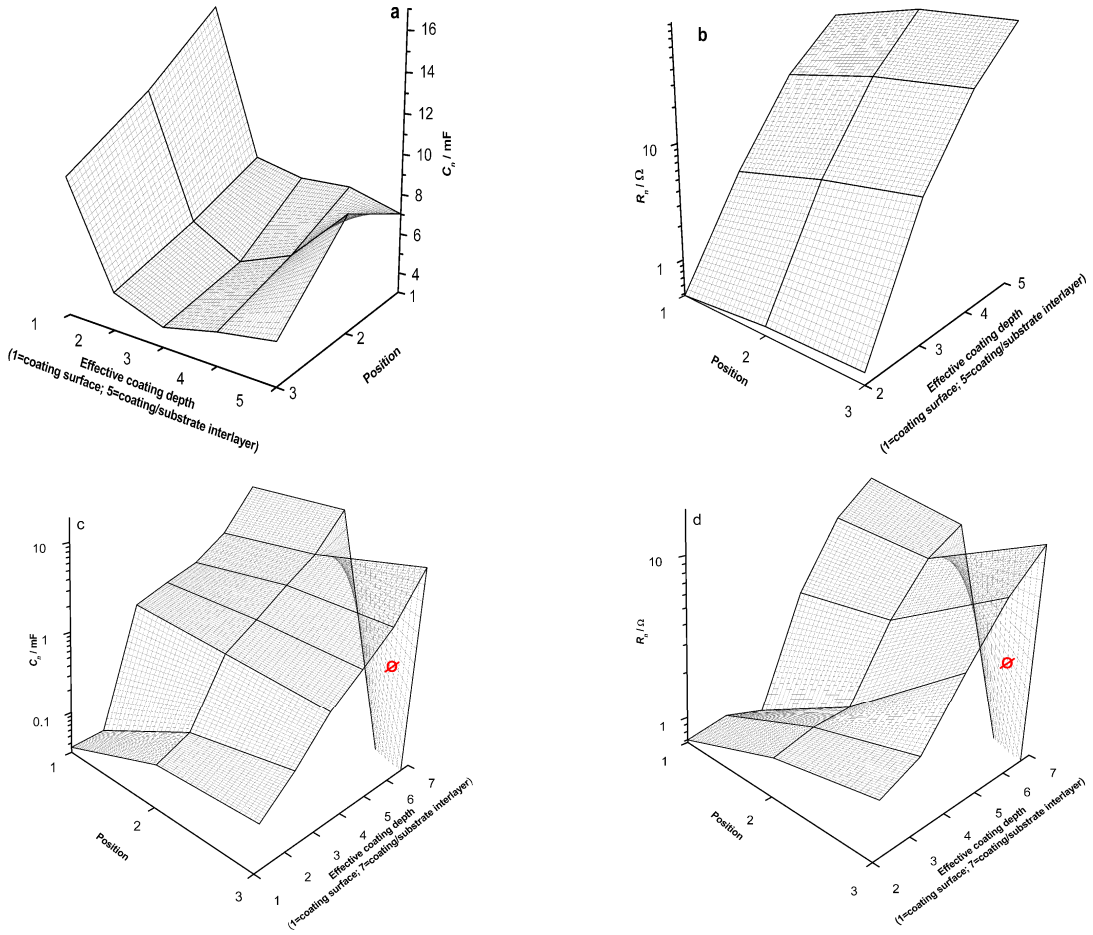

Figure 4. Surface (positions 1–3) and in-depth (effective coating depth) distribution of the coating capacitance (**a**,**c**) and pore resistance (**b**,**d**) through the coating layer of the as-prepared (**a**,**b**) and exhausted (**c**,**d**) oxygen-evolving electrode (effective coating depth correlated to the nth order of equivalent transmission line equivalent circuit). Here, 1 = coating surface, n = coating/substrate interface, and ∅ = no data for n = 7 at position 3 after the AST.

Another observation in Figure 4 additionally supports the proposed mechanism and concerns the comparison of surface capacitances (n = 1) among random surface positions. As also found in the CV analysis (Figure 2), the surface capacitance was highest at position 1 for the as-prepared state, which was accessible through the lowest pore resistance (Figure 4a,b). Although this difference in pore resistance with respect to the other two positions became even more pronounced during the AST (Figure 4d, n ≤ 4), which allowed easier access to the internal capacitance (which was by far the highest for position 1 at n = 4), and the surface capacitance was the lowest during the AST (Figure 4c, n ≤ 2). This shows that surface exhaustion of the coating's active material was the most pronounced and surface-localized at position 1. However, this behavior during the AST should not be expected, since the AST condition for position 1 was 2 A/cm^2, whereas the higher current of 3 A/cm^2 was applied to positions 2 and 3. The applied difference was intended to supply data for the influence of the AST-imposed current on the degradation mechanism of provisionally the same coating characteristics. The findings in Figure 4c were the opposite of the expectations, since higher AST currents should produce more vigorous gas evolution and consequently more pronounced inaccessibility to the coating interior (i.e., coating degradation more localized to its surface). According to Figure 4c, a lower AST current apparently affected the degradation at the coating's surface more than hindered accessibility to the coating interior at higher AST currents did. It could be that the lower pore resistance at position 1 allowed much easier evolution of the smaller gas bubbles,

(Their generation rate was below the critical value to allow extending above the critical bubble radius, approaching the pore radius.) which is beneficial for accessibility of the coating interior. These considerations additionally promote the unique requirement of careful planning of the active material's distribution through the coating toward the surface allocation, independent of whether the anode operational conditions would be moderate or vigorous.

Although it followed that an analysis of the CVs (Figure 2) did not supply information about the coating degradation in comparison with the EIS (except for a moderate tilt in the curves), there is other valuable information which can be gained from CV-EIS data correlation. The pseudocapacitive (PC) redox transition processes of noble metal oxides require the insertion (cathodic) or rejection (anodic) of H^+ [38], which takes place in a wider potential charging and discharging window applied in CV but not in EIS (rms amplitude of only 10 mV). The voltammetric capacitances from Figure 2d should hence contain a PC contribution of a much higher degree than the overall EIS capacitance through the n branches in Figure 4a,c. If the CV sweep rate as the input charging and discharging perturbation is low enough to penetrate the porous coating, as it would for the lowest input frequencies in EIS, then it can be assumed that a comparison of the CV-EIS capacitances can quantify the PC contribution. Since this contribution is strictly related to the number of active sites, the comparison of the CV-EIS data for the as-received coating at different positions can give insight into the coating composition's uniformity (Table 1).

Table 1. Total coating capacitance of as-prepared electrode before accelerated stability test ($\Sigma_{CEIS,ap}$) and after accelerate stability test ($\Sigma C_{EIS,ex}$); the relative contribution of the electrode surface capacitance ($\eta_{Surface}$); and the pseudocapacitive contribution to the total coating capacitance obtained from the difference between the total capacitance calculated from cyclic voltamograms and the total capacitance calculated from EIS ($\delta_{pc} = C_{CV} - \Sigma C_{EIS,ap}$). Calculations for negligible coating pore resistance ($R_n < 1$ and $n \leq 2$) are given in brackets. Data for three different positions are given in the table.

Parameter	Position 1	Position 2	Position 3
Before AST			
$\Sigma C_{EIS,ap}$/mF	48.4	38.8	27.6
$\Sigma C_{EIS,ap,S}$/mF ($n \leq 3(2)$, $R_n < 10(1)$ Ω)	33.5 (25.5)	24.4 (19.3)	18.2 (14.3)
After AST			
$\eta_{Surface}$, %	69 (53)	63 (50)	66 (52)
δ_{pc}/%	14	26	42
$\Sigma C_{EIS,ex}$/mF	25.9	31.1	18.4
$\Sigma\delta_{CEIS,ap\text{-}ex}$/%	47	20	33
δ_{pc}/%	76	57	112

The total coating capacitance through EIS was lower with respect to the voltametric capacitance, but this PC contribution in CV could be considerably different, depending on the coating structure and state. It follows that the PC contribution (δpc) is higher if the total EIS, as well as the voltametric capacitance, are lower (i.e., if the coatings are more compact, thick and of a smaller real surface area). The apparent exception is position 2 after the AST, which indicates that this position was the least compact one upon the AST's application, since position 1, found to be the least compact position in the as-prepared state, was exhausted the most by the AST at a lower current density. (This is also clearly indicated by the highest $\Sigma C_{EIS,ap\text{-}ex}$ value at position 1). Indeed, Figure 4d,c clearly shows that position 2 had the lowest pore resistance and highest capacitance for n = 5 and 6 after the AST.

Different PC contributions caused by the difference in coating structure now appear to be the main cause of the finding that CV was not able to register the difference between the

as-prepared and exhausted coating states. The same cause also affected the difference in capacitive performances among different surface positions. In CV, this difference was found to be below 20%, but in the EIS analysis, with a reduced PC contribution, it was found that the difference in total capacitance exceeded 25%, and it was even greater for the surface layers ($\Sigma_{CEIS,ap,S}$). This indicates that the nonuniformity in the coating morphology was more pronounced, especially for the surface texture, than the difference in PC performances affected by the structure of the active sites as well as their number.

The surface layers of the coating were thus found to be the main source of the coating's structural nonuniformity and consequently governed both the basic electrochemical performance and the mechanism of the loss of operational activity. Table 1 presents the values of the surface contribution to the total coating capacitance ($\eta_{Surface}$) down to a certain depth, taking the pore resistance value as the input perturbance limit for penetration. For negligible coating pore resistance ($R_n < 1\ \Omega$ for $n \leq 2$; Figure 3b) approximately 50% of the total available coating capacitance ($\Sigma C_{EIS,ap}$) was easily accessible and created the registered electrochemical performance. This was quite similar at all positions, which indicates that the coating was rather uniform with respect to the in-depth composition. (There was no segregation of the coating components). If the pore resistance increased up to 10 Ω (which appeared to be its order of magnitude for the exhausted anode), then the relative increase in the surface contribution was only about 15% on average and still similar at all positions. This confirms that the surface led the operation of the anode. Once the surface properties were lost under the AST, there was still roughly 50% of the coating which stayed intact, as was found via CV. However, it was hidden behind a considerably higher resistance, leading to spending higher voltages at the applied AST current densities.

The analyzed coating performances (basic and operational) also affected the coating activity for the oxygen evolution reaction (OER). Figure 5 shows the polarization curves at three different positions on the coating surface for the as-prepared and exhausted states. The data were made to compensate for IR drops to find the true OER activity and Tafel slopes (Figure 5a) and additionally normalized by the total EIS capacitance to reach the true values of the current densities (Figure 5b) (i.e., the rates of OER). The measured values of the Tafel slopes are given in Table 2.

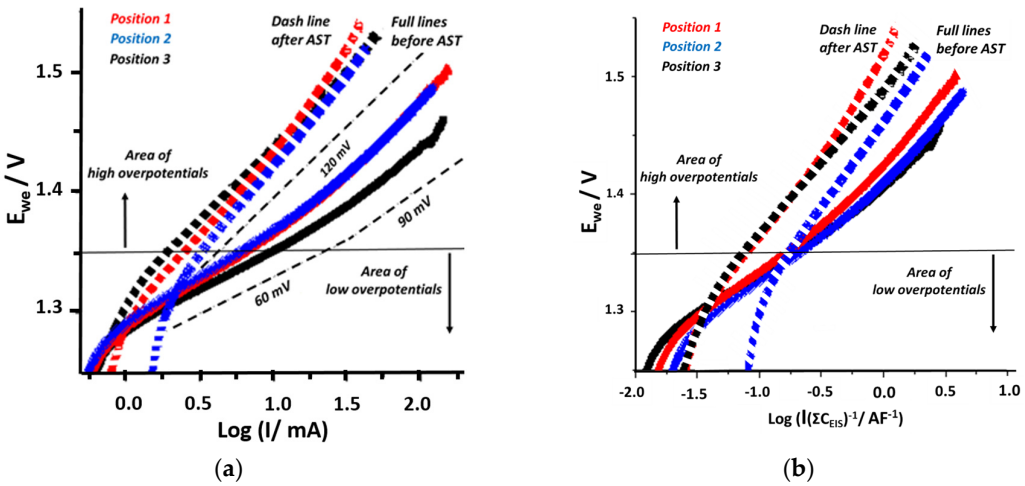

Figure 5. IR drop-corrected (**a**) and normalized (**b**) polarization curves for oxygen evolution reaction on IrO_2-Ta_2O_5 coating on Ti obtained before (full lines) and after (dash lines) an accelerated stability test (AST) in 10% H_2SO_4 at three different coating surface positions.

Table 2. Tafel slopes of all three positions before and after accelerated stability test (AST).

Position	Tafel Slope Before AST (mV dec^{-1}) (TS ± SD)	Tafel Slope After AST (mV dec^{-1}) (TS ± SD)
1	64 ± 0.1 Low overpotentials * 99 ± 0.5 High overpotentials **	123 ± 1
2	78 ± 0.4 Low overpotentials 131 ± 0.7 High overpotentials	143 ± 1
3	73 ± 0.1 Low overpotentials 126 ± 0.6 High overpotentials	143 ± 0.2

* Region of the low overpotential was below a potential of 1.35 V vs. SCE. ** Region of the high overpotential was above the potential of 1.35 V vs. SCE.

In accordance with the findings for CV and EIS, the least compact and possibly thickest part of the as-prepared coating (position 1 before the AST) appears to be the most active one (i.e., highest apparent current densities both at low and high OER overpotentials). The more compact positions (positions 2 and 3) showed almost identical activity, despite the differences in capacitive performances. If the total capacitance was taken as a measure of the real surface area to normalize the currents, then all positions were of similar OER activity levels, which indicates that the differences in the apparent currents in Figure 5a were due to differences in the coating texture and not the distributed nonuniform activity. A similar conclusion can also be reached if the Tafel slops are analyzed.

In the as-prepared state, the regions of low and high Tafel slopes were found at the negative (low OER overpotentials) and positive (high OER overpotentials) potentials at approximately 1.35 V_{SCE}, respectively. The slopes were close to the theoretical ones (60 and 90 or 120 mV) proposed for the reaction mechanisms of charge transfer or adsorption as rate-determining steps [35]. A unique slope for the exhausted coatings close to or higher than 120 mV was found. This suggests that the most probable slope in the electrocatalytic sense is 120 mV, whereas the halved value of 60 mV at low overpotentials could be due to halving of the activation energy according to the theory of electrocatalysis of porous electrodes [39]. Without delving into the details, it could be mentioned that at low overpotentials, the coating's behavior is porous until saturation of the pores with previously evolved and then dissolved oxygen. Upon saturation and an increase in the amount of evolved oxygen bubbles, which filled the pores at higher overpotentials, the coating's surface participated in the OER, behaving much like a flat electrode. This caused a transition from 60 mV for the porous structure to a "real" slope of 120 mV for a "flat" electrode. Since the exhausted coating had considerably wider pores (considerable decrease in pore resistance; Figure 4b,d), the condition of "electrocatalytic flattening" was not fulfilled, and a unique slope of 120 mV was registered.

These considerations also allow the existence of mixed porous and flat behavior in a high overpotential region if the pores and cracks are wide enough. This behavior can be assigned to the least compact position (position 1) for which the bubble evolution dynamics from the pores allow a great electrocatalytic contribution from the porous structure with a somewhat lower slope of about 90 mV (Figure 5a).

The investigation of the OER kinetics thus supports the findings of the analysis of the coating's electrochemical performances in CV and EIS (i.e., the way the coating texture is reflected by the capacitive and electrocatalytic properties) as well as the coating operation in electrolysis and, consequently, the service life and exhaustion state.

4. Conclusions

The standard electrochemical performances of the oxygen-evolving anode IrO_2-Ta_2O_5/Ti were investigated through capacitive behavior at constant perturbation dynamics through cyclic voltammetry (CV), discontinuous dynamics under electrochemical impedance spectroscopy (EIS) and electrocatalytic activity for oxygen evolution reactions (OERs) via polarization measurements. Performance (non)uniformity was checked over the surface

and through the depth of the coating at three different positions on the coating's surface. For in-depth coating performance profiling, the approach of distributed time constants due to time-dependent electrical perturbation was applied. Since the aim was to correlate the texture and uniformity of a coating and its performance to define a pathway for the anode's operational disfunction during the side water electrolysis of the metal electrowinning process, the coating was analyzed in its as-prepared and exhausted states.

More than half of the quantified coating electrochemical activity was found to be related to its surface layers, which also suffered from a considerable loss of activity upon anode disfunction via electrolysis. The performances of the coating interior were affected only negligibly. This finding held for different coating textures, morphologies and electrolysis operational conditions, as it was found to be characteristic of coating nonuniformity due to the thermal procedure of coating formation through drop casting deposition in separate layers. As a guideline for the generation of more efficient coatings, the findings clearly suggest a modified procedure for the distributed composition of deposited layers with top coating layers more rich in the active component IrO_2.

Correlation of CV-EIS and OER activity data also indicate that more porous and cracked surface layers, which are more likely to be generated if the coatings are thicker, are more electrochemically efficient, being able to allow the coating to operate more uniformly in electrolysis. In other words, a more porous and thicker coating with a surface enriched by the active component should have a longer service life and better and more uniform material efficiency.

Author Contributions: Conceptualization, V.P. and G.Š.; methodology, V.P. and G.Š.; software, J.B.; validation, V.P., G.Š. and B.G.; formal analysis, V.P. and J.B.; investigation, J.B. and G.Š.; resources, J.S. and S.S.; data curation, V.P. and J.B.; writing—original draft preparation, V.P. and J.B.; writing—review and editing, J.B., V.P. and G.Š.; visualization, J.B. and M.S.; supervision, B.G. and G.Š.; project administration, V.P.; funding acquisition, J.S. and S.S. All authors have read and agreed to the published version of the manuscript.

Funding: The authors wish to acknowledge the support of the Science Fund of the Republic of Serbia (project number 6666), Renewal of the Waste Oxygen-Evolving anodes from Hydrometallurgy and their improved Activity for Hydrogen Economy, Wastewater and Soil Remediation—OxyRePair.

Data Availability Statement: The original contributions presented in the study are included in the article, further inquiries can be directed to the corresponding author.

Conflicts of Interest: The authors declare no conflicts of interest.

References

1. Belal, R.M.; Zayed, M.A.; El-Sherif, R.M.; Abdel Ghany, N.A. Advanced electrochemical degradation of basic yellow 28 textile dye using IrO_2/Ti meshed electrode in different supporting electrolytes. *J. Electrochem. Soc.* **2021**, *882*, 114979. [CrossRef]
2. Ma, R.; Cheng, S.; Zhang, X.; Li, S.; Liu, Z.; Li, X. Oxygen evolution and corrosion behavior of low-MnO_2-content Pb-MnO_2 composite anodes for metal electrowinning. *Hydrometallurgy* **2016**, *159*, 6–11. [CrossRef]
3. Bebelis, S.; Bouzek, K.; Cornell, A.; Ferreira, M.G.S.; Kelsall, G.H.; Lapicque, F.; de León, C.P.; Rodrigo, M.A.; Walsh, F.C. Highlights during the development of electrochemical engineering. *Chem. Eng. Res. Des.* **2013**, *91*, 1998–2020. [CrossRef]
4. Han, Z.; Zhu, P.; Xu, L.; Kannan, C.S.; Guo, S.; Liu, J.; Koppala, S.; Ju, S. Electrochemical properties of the IrO_2-Ta_2O_5 coated anodes with Al/Ti and Cu/Ti layered composites substrates. *J. Alloys Compd.* **2018**, *769*, 210–217. [CrossRef]
5. Cao, H.; Zhang, L.; Chen, M. Characteristics of anodic TiO_2 nanotube arrays mediated IrO_2 Active Anode in the Oxygen Evolution Reaction. *Int. J. Electrochem. Sci.* **2022**, *17*, 220461. [CrossRef]
6. Dondapati, J.S.; Thiruppathi, A.R.; Salverda, A.; Chen, A. Comparison of Pt and IrO_2-Ta_2O_5/Ti as a counter electrode in acidic media. *Electrochem. commun.* **2021**, *124*, 106946. [CrossRef]
7. Trasatti, S. *Electrodes of Conductive Metallic Oxides*, 1st ed.; Elsevier Scientific Publishing Company: Amsterdam, The Netherlands, 1980; p. 702.
8. Kawaguchi, K.; Morimitsu, M. Reaction Selectivity of IrO_2-Based Nano/Amorphous Hybrid Oxide-Coated Titanium Anodes in Acidic Aqueous Solutions: Oxygen Evolution and Lead Oxide Deposition. *J. Electrochem. Soc.* **2020**, *167*, 133503. [CrossRef]
9. Kasian, O.; Li, T.; Mingers, A.M.; Schweinar, K.; Savan, A.; Ludwig, A.; Mayrhofer, K. Stabilization of an iridium oxygen evolution catalyst by titanium oxides. *J. Phys. Energy* **2021**, *3*, 034006. [CrossRef]
10. Trasatti, S. Electrocatalysis: Understanding the success of DSA®. *Electrochim. Acta* **2000**, *45*, 2377–2385. [CrossRef]

11. Kotz, R.; Stucki, S. Stabilization of RuO_2, by IrO_2, for anodic oxygen evolution in acid media. *Electrochim. Acta* **1986**, *31*, 1311–1316. [CrossRef]
12. Kamegaya, Y.; Sasaki, K.; Oguri, M.; Asaki, T.; Kobayashi, H.; Mitamura, T. Improved durability of iridium oxide coated titanium anode with interlayers for oxygen evolution at high current densities. *Electrochim. Acta* **1995**, *40*, 889–895. [CrossRef]
13. Tang, D.; Wen, S.; Chen, S. Preparation and characterization for a RuO_2 60%-TiO_2 40% nano-material. *Transc. Met. Heat Treat.* **2000**, *21*, 12–16.
14. Kim, M.; Choi, J.; Lee, W.; Ahn, Y.; Lee, H.; Cho, K.; Lee, J. Performance of Magnéli phase Ti_4O_7 and Ti^{3+} self-doped TiO_2 as oxygen vacancy-rich titanium oxide anodes: Comparison in terms of treatment efficiency, anodic degradative pathways, and long-term stability. *Appl. Catal. B Environ.* **2023**, *337*, 122993. [CrossRef]
15. Mirseyed, S.F.; Jafarzadeh, K.; Rostamian, A.; Abbasi, H.M.; Ostadhassan, M. A new insight on the mechanisms of corrosion deactivation of a typical Ti/IrO_2 + RuO_2+TiO_2 coating in the presence of Ta_2O_5 in chlor-alkali medium. *Corros. Sci.* **2023**, *214*, 111005. [CrossRef]
16. Rosestolato, D.; Neodo, S.; Ferro, S.; Battaglin, G.; Rigato, V.; De Battisti, A. A comparison between structural and electrochemical properties of iridium oxide-based electrocatalysts prepared by sol-gel and reactive sputtering deposition. *J. Electrochem. Soc.* **2014**, *161*, 151–158. [CrossRef]
17. Herrada, R.A.; Acosta-Santoyo, G.; Sepúlveda-Guzmán, S.; Brillas, E.; Sirés, I.; Bustos, E. IrO_2-Ta_2O_5 | Ti electrodes prepared by electrodeposition from different Ir:Ta ratios for the degradation of polycyclic aromatic hydrocarbons. *Electrochim. Acta* **2018**, *263*, 353–361. [CrossRef]
18. Yang, C.; Shang, S.; Li, X. Oxygen-vacancy-enriched substrate-less SnOx/La-Sb anode for high-performance electrocatalytic oxidation of antibiotics in wastewater. *J. Hazard. Mater.* **2022**, *436*, 129212. [CrossRef]
19. Comninellis, C.; Vercesi, G.P. Characterization of DSA-type oxygen evolving electrodes: Choice of a coating. *J. Appl. Electrochem.* **1991**, *21*, 335–345. [CrossRef]
20. Lee, J.Y.; Kang, D.K.; Lee, K.; Chang, D. An investigation on the electrochemical characteristics of Ta_2O_5-IrO_2 anodes for the application of electrolysis process. *Mater. Sci. Appl.* **2011**, *2*, 237–243.
21. Xu, W.; Haarberg, G.M.; Seland, F.; Sunde, S.; Ratvik, A.P.; Holmin, S.; Gustavsson, J.; Afvander, Å.; Zimmerman, E.; Åkre, T. The durability of the thermally decomposed IrO_2-Ta_2O_5 coated titanium anode in a sulfate solution. *Corros. Sci.* **2019**, *150*, 76–90. [CrossRef]
22. Herradaa, R.A.; Rodilb, S.E.; Sepúlveda-Guzmánc, S.; Manríqueza, J.; Exnerd, K.S.; Bustosa, E. Characterization of Ti electrodes electrophoretically coated with IrO_2-Ta_2O_5 films with different Ir:Ta molar ratios. *J. Alloys Compd.* **2021**, *862*, 158015. [CrossRef]
23. Xu, L.; Xin, Y.; Wang, J. A comparative study on IrO_2-Ta_2O_5 coated titanium electrodes prepared with different methods. *Electrochim. Acta* **2009**, *54*, 1820–1825. [CrossRef]
24. Herrada, R.A.; Medel, A.; Manríquez, F.; Sirés, I.; Bustos, E. Preparation of IrO_2-Ta_2O_5 | Ti electrodes by immersion, painting and electrophoretic deposition for the electrochemical removal of hydrocarbons from water. *J. Hazard. Mater.* **2016**, *319*, 102–110. [CrossRef]
25. Kawaguchi, K.; Morimitsu, M. Effects of oxide composition on structure, surface morphology, and oxygen evolution behaviors of IrO_2-Ta_2O_5/Ti anodes prepared at a high temperature. *Electrochemistry* **2015**, *83*, 256–261. [CrossRef]
26. Xu, W.; Haarberg, G.M.; Sunde, S.; Seland, F.; Ratvik, A.P.; Holmin, S.; Gustavsson, J.; Afvander, Å.; Zimmerman, E.; Åkre, T. Sandblasting effect on performance and durability of Ti based IrO_2-Ta_2O_5 anode in acidic solutions. *Electrochim. Acta* **2019**, *295*, 204–214. [CrossRef]
27. Guzmána, D.; Dubraya, G.; Aguilarb, C.; Rojasc, P.; Guzmána, A.; Soliz, Á.; Sepúlvedaa, R.; Espinozad, R. Mechanochemical processing of IrO_2–Ta_2O_5: An alternative route for synthesizing Ir and Ir(Ta)O_2 solid solution. *Boletín Soc. Española Cerámica Vidr.* **2021**, *60*, 109–118. [CrossRef]
28. Martelli, G.; Ornelas, R.; Faita, G. Deactivation mechanisms of oxygen evolving anodes at high current densities. *Electrochim. Acta* **1994**, *39*, 1551–1558.
29. Jansen, H.J.; Mackor, A. Anodes with Extended Service Life and Methods for Their Manufacturing. EPO Patent No. 0538955B1, 1998.
30. Yan, Z.; Zhang, H.; Feng, Z.; Tang, M.; Yuan, X.; Tan, Z. Promotion of in situ TiNx interlayer on morphology and electrochemical properties of titanium based IrO_2-Ta_2O_5 coated anode. *J. Alloys Compd.* **2017**, *708*, 1081–1088. [CrossRef]
31. Liu, B.; Ma, B.; Chen, Y.; Wang, C. Corrosion mechanism of Ti/IrO_2-RuO_2-SiO_2 anode for oxygen evolution in sulfuric acid solution. *Corros. Sci.* **2020**, *170*, 108662. [CrossRef]
32. Liu, Y.; Xu, L.; Xuan, J.; Xin, Y.; Li, Y.; Duan, T.; Liu, F. A comparative study on Ti/IrO_2–Ta_2O_5 anodes prepared by microwave plasma-assisted sintering and conventional thermal decomposition methods. *J. Mater. Res. Technol.* **2023**, *23*, 1447–1457. [CrossRef]
33. Mehdipour, M.; Tabaian, S.H.; Firoozi, S. Effect of IrO_2 crystallinity on electrocatalytic behavior of IrO_2–Ta_2O_5/MWCNT composite as anodes in chlor-alkali membrane cell. *Ceram. Int.* **2019**, *45*, 19971–19980. [CrossRef]
34. Wang, Y.; Tong, H.; Xu, W. Electrocatalytic activity of Ti/TiO_2 electrodes in H_2SO_4 solution. *Chin. J. Process. Eng.* **2003**, *3*, 356–360.
35. Ren, Z.; Quan, S.; Gao, J.; Li, W.; Zhu, Y.; Liu, Y.; Chai, B.; Wang, Y. The electrocatalytic activity of IrO_2–Ta_2O_5 anode materials and electrolyzed oxidizing water preparation and sterilization effect. *RSC Adv.* **2015**, *5*, 8778–8786. [CrossRef]
36. Panić, V.; Dekanski, A.; Mišković-Stanković, V.B.; Milonjić, S.; Nikolić, B. On the deactivation mechanism of RuO_2–TiO_2/Ti anodes prepared by the sol–gel procedure. *J. Electroanal. Chem.* **2005**, *579*, 67–76. [CrossRef]

37. Conway, B.E. *Electrochemical Supercapacitors: Scientific Fundamentals and Technological Applications*; Springer Science + Business Media, LLC.: New York, NY, USA, 1999; pp. 221–257.
38. Gileadi, E. Simultaneous two-electron transfer in electrode kinetics. *J. Electroanal. Chem.* **2002**, *532*, 181–189. [CrossRef]
39. Chizmadzhevand, Y.A.; Chirkov, Y.G. Porous Electrodes. In *Comprehensive Treatise of Electrchemistry*, 1st ed.; Yeager, E., Bockris, J.O.M., Conway, B.E., Sarangapani, S., Eds.; Springer Science + Business Media: New York, NY, USA, 1983; Volume 6, pp. 317–385.